

2D Probabilistic Undersampling Pattern Optimization for MR Image Reconstruction

Shengke Xue, Ruiliang Bai, and Xinyu Jin

Abstract—Magnetic resonance imaging (MRI) is mainly limited by long scanning time and vulnerable to human tissue motion artifacts, in 3D clinical scenarios. Thus, k -space undersampling is used to accelerate the acquisition of MRI while leading to visually poor MR images. Recently, some studies 1) use effective undersampling patterns, or 2) design deep neural networks to improve the quality of resulting images. However, they are considered as two separate optimization strategies. In this paper, we propose a cross-domain network for MR image reconstruction, in a retrospective data-driven manner, under limited sampling rates. Our method can simultaneously obtain the optimal undersampling pattern (in k -space) and the reconstruction model, which are customized to the type of training data, by using an end-to-end learning strategy. We propose a 2D probabilistic undersampling layer, to obtain the optimal undersampling pattern and its probability distribution in a differentiable way. We propose a 2D inverse Fourier transform layer, which connects the Fourier domain and the image domain during the forward pass and the backpropagation. In addition, by training 3D fully-sampled k -space data and MR images with the traditional Euclidean loss, we discover the universal relationship between the probability distribution of the optimal undersampling pattern and its corresponding sampling rate. Experiments show that the quantitative and qualitative results of recovered MR images by our 2D probabilistic undersampling pattern obviously outperform those of several existing sampling strategies.

Index Terms—Magnetic resonance imaging, undersampling, cross-domain, reconstruction, probability distribution, deep learning.

I. INTRODUCTION

MAGNETIC resonance imaging (MRI) is one of the crucial tools for medical research, disease analysis, and clinical diagnosis, due to its non-invasiveness, non-ionizing radiation, and outstanding contrast. However, the long acquisition time is a primary drawback that limits the applications of MRI. Parallel imaging that relies on the multi-coil technology is useful to accelerate the MRI, at the cost of hardware requirements. An alternative technique is compressed sensing (CS), because CS overcomes the limitation of the Nyquist-Shannon sampling law with the nature of redundancy in k -space. To this end, recovering a high-quality MR image from its partial undersampled k -space data becomes feasible. This property is quite suitable for accelerating the acquisition of

MRI without hardware modification and hereby derives a series of CS-MRI algorithms, e.g., total variation (TV) [1], k - t FOCUSS [2], nuclear norm [3], [4] and low-rank completion [5]–[8] methods.

Since the sparse transforms mentioned above are primitive, dictionary learning [9] strategy has been used to iteratively represent signals by the sparse basis and its coefficients. CS-MRI process also integrates the idea of dictionary learning, using image patches to train sparse dictionary elements [10], [11]. However, this strategy is unstable, and the performance varies dramatically for different kinds of data. Especially for high-resolution images, a large-scale dictionary and a vast number of iterations are required to obtain the approximately optimal solution. Alternating direction method of multipliers (ADMM) has been introduced to CS-MRI, to further accelerate the process of sparse coding [12]. The traditional CS-MRI methods require that the acquisition matrix and the sparse transformation matrix are irrelevant, which is too difficult to satisfy in real scenarios. If the sparse basis is too simple, it is impossible to capture sophisticated tissue details in an MR image. TV-based sparse transformation can enhance the constraints for reconstructed MR images, but it will cause step artifacts. Wavelet transform can deal with singular points and isotropic features, but orthogonal Wavelet processing may lead to blocky artifacts in MR images. These methods are considered as non-linear optimization problems, while most of them are non-convex. They have to use numerous iterations and a great deal of time to converge, which can be computationally expensive. This indicates that they are not applicable for large-scale datasets.

Currently, deep learning has been widely used for MRI reconstruction. These studies can be roughly divided into four categories:

- 1) As shown in Fig. 1a, these methods use the inverse Fourier transform to deal with the undersampled k -space data, then they develop various architectures (e.g., residual network [13], [14], U-Net [15], or GAN [16], [17]) to improve the quality of reconstructed MR images. However, these methods ignore the influence of missing k -space data, and only design deep and wide structures to enhance the feature extraction capabilities. This kind of methods are regarded as the image post-processing schemes.
- 2) As shown in Fig. 1b, these methods [18], [19] also use the post-processing scheme, directly using undersampled k -space data (or MR images) as input. In addition, they

Corresponding author: Ruiliang Bai (ruiliangbai@zju.edu.cn)

S. Xue and X. Jin are with the College of Information Science and Electronic Engineering, Zhejiang University, Hangzhou, P. R. China (e-mail: xueshengke@zju.edu.cn, jinxny@zju.edu.cn).

R. Bai is with the *****, Zhejiang University, Hangzhou, P. R. China (e-mail: ruiliangbai@zju.edu.cn)

This work was supported by ***

Manuscript received *** **, 2020; revised *** **, 2020.

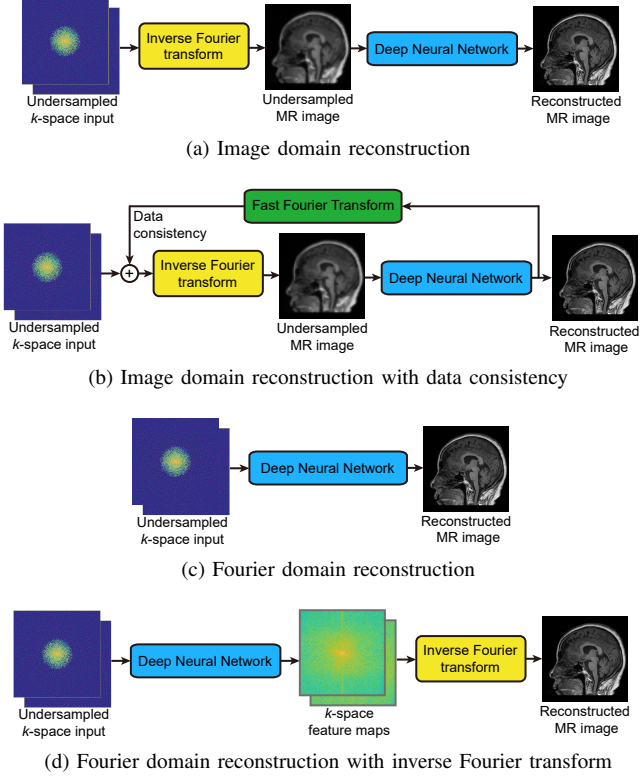


Fig. 1. Four types of deep learning based MRI reconstruction methods

incorporate the data consistency operation, i.e.,

$$u(k_x, k_y) = \begin{cases} s(k_x, k_y), & \text{if } (k_x, k_y) \notin \Omega, \\ \frac{s(k_x, k_y) + \lambda s_0(k_x, k_y)}{1+\lambda}, & \text{if } (k_x, k_y) \in \Omega, \end{cases} \quad (1)$$

where λ controls the importance of the original k -space data, and Ω denotes the set of points in the sampling pattern. These methods indicate that the known k -space data should be constant during training, and they use the feedback mechanism to iteratively update the missing k -space data in the Fourier domain.

- 3) As shown in Fig. 1c, these methods [20], [21] directly reconstruct MR images from the undersampled k -space data. They adopt the fully-connected (FC) network to replace the inverse Fourier transform. This obviously increases the number of parameters and requires a large amount of memory, since MR images usually have large dimensions. Besides, training the FC network with huge parameter numbers is hard to converge. Thus, these methods are only suitable for small-scale image sets.
- 4) As shown in Fig. 1d, this method [22] only designs the network in the Fourier domain, to recover the missing k -space data. Then the inverse Fourier transform is directly adopted to generate the final MR image. The drawback is that the network architecture in the Fourier domain is quite different from that in the image domain. The commonly-used expertise about depth, width, and kernel size is not effective in the Fourier domain. This apparently impedes the reconstruction performance.

The four types of deep learning based methods focus on developing deep neural networks, to improve the quality of

reconstructed MR images. However, they just take the undersampled partial k -space data as input, and do not consider the undersampling process as one part of the optimization framework. They usually adopt existing undersampling strategies, e.g., Cartesian undersampling, radial undersampling, or spiral undersampling. Besides, these methods do not provide enough theoretical proof, or analyze the undersampling strategy that is universal or customized to specific k -space data.

Since the model's performance is heavily dependent on the type of undersampling strategy, a few researches optimize the undersampling patterns to recover high-quality MR images in the data-driven fashion, which will be introduced in Section II-B. However, they have several drawbacks:

- 1) In real cases, sampling points are binary values and non-differentiable, which means that gradient backpropagation cannot be directly applied in training;
- 2) Integrating the underlying property (rule) of k -space data with the feature extraction capabilities of deep neural networks during training is difficult;
- 3) Optimal undersampling pattern and its corresponding theoretical expression cannot be simultaneously discovered from limited amount of k -space data.

To this end, we propose a cross-domain network for 2D undersampling pattern optimization and MR image reconstruction, in a retrospective data-driven fashion, under limited sampling rates (accelerating ratios). The major contributions of this paper include:

- We propose a 2D probabilistic undersampling layer, including differentiable probability and sampling matrices, to obtain the optimal undersampling pattern and analyze its corresponding probability distribution, which are customized to specific k -space data.
- We propose a 2D inverse Fourier transform layer, to achieve the cross-domain scheme. Specifically, the forward pass from the Fourier domain to the image domain and the backpropagation in the inverse direction can be established. To this end, our method simultaneously learns the optimal undersampling pattern (in the Fourier domain) and the reconstruction model (in the image domain), in an end-to-end training strategy.
- We discover the universal relationship between the probability distribution of our 2D undersampling pattern and its sampling rate, constrained to the traditional Euclidean loss, by training limited amount of 3D fully-sampled k -space data and MR images. Thus, our results can provide theoretical basis for different MRI 3D scanning scenarios.
- Experiments show that, under the same sampling rates, the quantitative and qualitative results of recovered MR images by our 2D probabilistic undersampling pattern noticeably outperform those of several existing sampling strategies.

The remainder of this paper is organized as follows. Section II introduces the MR image reconstruction related studies. Section III shows the entire framework of our cross-domain model. Section IV states detailed configurations for training our method. Experiments in Section V illustrate the results of our optimal undersampling pattern and provide the analysis

of its probability distribution. Section VI summarizes the conclusion and future directions.

II. RELATED WORK

A. Deep Learning for MR Image Reconstruction

Deep learning based CS-MRI methods aim to design deep networks to effectively recover MR images from undersampled partial k -space data [23]–[26].

Wang et al. [18] adopted the convolutional neural network (CNN) structure to train MR images, and built the mapping between the zero-filled undersampled MR images and fully-sampled MR images. After training, their model removed some artifacts caused by the zero-filling operation. Yang et al. [27] proposed the ADMM-Net, which combined ADMM with the CNN structure, to iteratively optimize their CS-MRI model. This method took the undersampled k -space data as input and adopted the 2D radial undersampling pattern. As a typical image post-processing scheme, Sun et al. [13] integrated the recursive learning, dilated convolution, and residual learning strategies, to deal with MR images that were undersampled by 30% one-dimensional (1D) Cartesian pattern. Schlemper et al. [19] proposed the deep cascade CNN model, which recovered the sequence of 2D cardiac MR images by using the 1D Cartesian undersampling pattern.

Yang et al. [16] proposed the deep de-aliasing generative adversarial network (DAGAN) for CS-MRI reconstruction. Here, the generator adopted the U-Net [28] structure and adopted the DCGAN for the discriminator. Yang et al. combined the pixel-wise loss, frequency-domain loss, perceptual loss, and adversarial loss as the joint constraints to train their model. Note that DAGAN adopted existed 2D Gaussian and Poisson undersampling patterns and did not optimize them in training. Similarly, Mardani et al. [29] proposed the GANCS model, applying the least-square GAN structure to CS-MRI reconstruction. By training deep residual networks with skip connections, the generator projected the MR image into manifold learning to suppress the artifacts. GANCS only adopted the 2D radial undersampling pattern with fixed angles to select k -space data. To avoid the complex values, DAGAN and GANCS both separated the real and imaginary components, concatenated them as two channels, and then fed them to their model for training. This strategy has been continuously adopted by subsequent studies.

Quan et al. [17] proposed the RefineGAN model, to achieve CS-MRI reconstruction. They combined the fully-residual convolutional auto-encoder with the CycleGAN [30], and designed the cyclic data consistency loss to effectively update missing k -space data in the Fourier domain. Hyun et al. [15] adopted the U-Net [28] for fast MRI reconstruction. They used the uniform undersampling strategy in the phase encoding direction of k -space data, and kept a little extra low-frequency (LF) data to weaken the aliasing artifacts. Hun et al. also adopted the data consistency operation, which aimed to preserve known k -space data and iteratively fill partial missing k -space data during training.

As mentioned above, deep learning has shown its advantages in CS-MRI reconstruction tasks. They obviously reduce

the running time of k -space undersampling and reconstruction, and significantly improve the quality of final MR images. However, the robustness of different types of k -space data and undersampling patterns has not been proved yet.

B. Optimization of the Undersampling Pattern

Recently, a few studies focus on the optimization of undersampling patterns [31]–[34] in a data-driven manner.

Gözcü et al. [31] proposed the parameter-free greedy mask selection (PFGMS) method, which used the progressive updating scheme to search the best undersampling pattern that performed well in MRI reconstruction. Since no adjustable parameters were used in the learning process, PFGMS had to greedily select masks in each iteration. Thus, this method required a great deal of time for numerous iterations, and could not be applied for large-scale datasets. Besides, PFGMS optimized the undersampling pattern and trained the cascade CNN [19] separately, by alternating two steps to obtain the approximately optimal solution. However, we propose the 2D probabilistic undersampling strategy to accelerate the optimization of undersampling patterns. Our cross-domain training scheme can simultaneously obtain parameters in the Fourier domain and image domain.

Huijben et al. [32] proposed the deep probability sampling (DPS) method, which adopted the two-layer FC network, three-layer CNN, or GAN to achieve the end-to-end training scheme. However, Huijben et al. only used the small-scale MNIST¹ and Cifar-10² datasets for training and validation, and did not test on MR image sets. To overcome the limitation of non-differentiable sampling issues, DPS introduced the Gumbel-softmax as a continuous differentiable relaxation, which still was not equal to binary sampling values. This strategy only chose the first k sampling points with the largest probability values, and ignored most high-frequency (HF) information. However, our 2D probabilistic undersampling scheme solves the non-differentiable problem and is equivalent to real binary undersampling process. In addition, we can provide the probability distribution of undersampling as the theoretical basis.

Aggarwal et al. [33] proposed the joint model-based deep learning (J-MoDL) method for optimizing undersampling and reconstruction. They adopted the undersampling in horizontal and vertical directions, k -space data consistency operation, and the U-Net structure. However, Aggarwal et al. used a complicated training strategy: 1) training the U-Net only; 2) training the undersampling pattern only; 3) training both of them. This strategy was quite inefficient and contained plenty of redundant computation. To make the undersampling pattern differentiable in backpropagation, J-MoDL directly replaced binary sampling points with continuous values, which was quite different from the actual undersampling process. Thus, the results of J-MoDL were not useful in real undersampling cases. In addition, the undersampling pattern of J-MoDL allocated the sampling points uniformly to the LF and HF parts, regardless of the importance distribution of k -space

¹<http://yann.lecun.com/exdb/mnist/>

²<https://www.cs.toronto.edu/%7Ekriz/cifar.html>

data. Besides, no theoretical analysis was provided for their undersampling patterns. However, in this paper, we solve the non-differentiable issue of the undersampling pattern and discover its probability distribution.

Bahadir et al. [35] proposed the learning-based optimization of the undersampling pattern (LOUP) in MRI. They adopted the probabilistic mask p and binary mask m to learn the underlying pattern in undersampling. However, to make their loss differentiable, they applied the sigmoid function on p to approximate the step function, which was not equivalent to binary values (0 / 1). Their mask required special initialization: having a fixed 32×32 rectangular region sampled in the center of the k -space, based on the sampling prior expertise to reduce artifacts. The final masks of LOUP were quite similar to our results in Section V-F, but Bahadir et al. did not consider the stable constraint or conduct any theoretical analysis for their undersampling patterns.

Weiss et al. [34] proposed the joint learning of 1D Cartesian undersampling and reconstruction (J-CUR) method. Similar to our probabilistic undersampling strategy, Weiss et al. designed the binary mask vector Φ and continuous mask vector Φ_c . In each iteration, they used Φ_c to update Φ by using hard threshold τ . Its corresponding forward pass and backpropagation were similar to our schemes. The difference is that Weiss et al. adopted the hard threshold, leading to inflexible undersampling patterns, but we adopt the independent identically distributed (i.i.d) probability distribution to generate the status of each sampling points. Moreover, the initialization of vectors Φ and Φ_c were pretty sophisticated: manually setting the specific sampling rates to the LF and HF components. As a result, the undersampling pattern did not change explicitly in training, and Φ_c was not considered as the probability distribution for analysis, either. Besides, J-CUR method only used an ℓ_1 loss, resulting in insufficient supervised constraints during training, so that it could not obtain the optimal undersampling pattern and final MR images.

III. CROSS-DOMAIN OPTIMIZATION FRAMEWORK

In this paper, the proposed cross-domain framework includes three parts: the 2D probabilistic undersampling layer, the 2D inverse Fourier transform layer, and the reconstruction network.

A. 2D Probabilistic Undersampling Layer

To simulate the process of k -space undersampling in real scenarios, we propose the 2D probabilistic undersampling layer, as shown in Fig. 2, where the input are the fully-sampled k -space data (real and imaginary parts). After undersampling, the output of this layer are the undersampled k -space data, then it can be passed to the next layer. To keep the data format and dimension consistent in training, we separate the real and imaginary parts as two matrices, then concatenate them as two channels. This can be expressed as:

$$\hat{\mathbf{X}}_{\text{in}} = [\text{real}(\mathcal{K}), \text{imag}(\mathcal{K})] \in \mathbb{R}^{m \times n \times 2}. \quad (2)$$

This strategy [17], [19], [22] can avoid the computation of complex numbers and is convenient to implement in some main-stream frameworks.

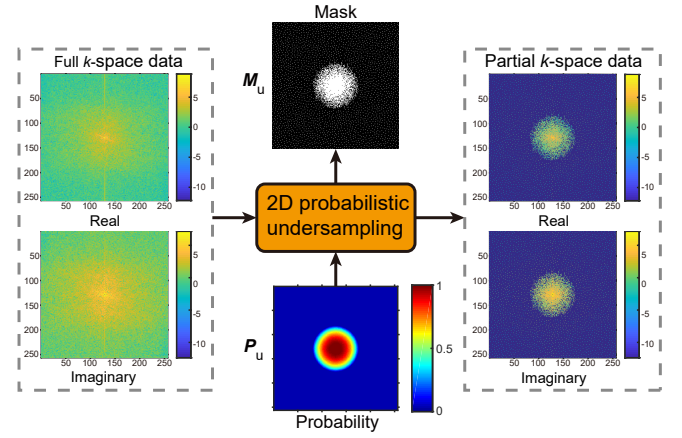


Fig. 2. Proposed 2D probabilistic undersampling layer: P_u is the probability matrix; M_u is the sampling matrix

In this paper, the undersampling process is realized by the Hadamard product, which is respectively applied to the real and imaginary parts, as shown in Fig. 2 and Eq. (3):

$$\begin{aligned} \hat{\mathbf{X}}_{\text{in}} &= \hat{\mathbf{X}}_{\text{in}} \circ M_u \\ &= [\text{real}(\mathcal{K}) \circ M_u, \text{imag}(\mathcal{K}) \circ M_u] \in \mathbb{R}^{m \times n \times 2}, \end{aligned} \quad (3)$$

where “ \circ ” denotes the Hadamard product, and $M_u \in \mathbb{R}^{m \times n}$ denotes the sampling matrix, which has the same dimension as k -space data and ranges from binary values {0, 1}. Here, “0” denotes the unused part, shown as the black area in the “mask” of Fig. 2; “1” denotes the sampled part, shown as the white area in the “mask” of Fig. 2, i.e. the set of all points in the undersampling pattern. The effect of the Hadamard product is equivalent to preserving partial k -space data by the sampling matrix M_u and discarding other parts, then filled with zeros. To this end, the dimension of output is the same as its input, but only limited rate of k -space data exist. The sampling rate is defined as the number of sampling points in M_u divided by the total number of elements in M_u .

Instead of directly using previous undersampling patterns, we propose a probability matrix, denoted as $P_u \in \mathbb{R}^{m \times n}$, ranging from the continuous interval [0, 1]. By applying the Bernoulli distribution to each element of P_u , we obtain

$$\mathcal{B}(1, p = P_u(x, y)) = \begin{cases} \mathcal{B}(M_u(x, y) = 1) = p, \\ \mathcal{B}(M_u(x, y) = 0) = 1 - p. \end{cases} \quad (4)$$

In this manner, we update each element of M_u by P_u . Every $M_u(x, y)$ follows the Bernoulli distribution with probability $P_u(x, y)$, and they are all independently distributed. Similarly, $P_u(x, y)$ can be considered as the indicator of the importance at the point $M_u(x, y)$. Thus, only P_u is trainable in our 2D probabilistic undersampling layer. Because the values in M_u are binary (either “0” or “1”) in forward pass, they are natively non-differentiable and have no gradient in backpropagation. Section IV-A will provide our solution to this issue.

B. Inverse Fourier Transform Layer

To connect the Fourier domain with the image domain, we design the 2D inverse Fourier transform layer. Since the input

of this layer are the undersampled k -space data, we obtain the undersampled MR images by using the inverse Fourier transform. The forward and inverse process can be expressed as:

$$\hat{\mathbf{X}}_u(u, v) = \sum_{x=0}^{m-1} \sum_{y=0}^{n-1} \mathbf{X}_u(x, y) e^{-i2\pi(\frac{ux}{m} + \frac{vy}{n})}, \quad (5)$$

$$\mathbf{X}_u(x, y) = \frac{1}{mn} \sum_{u=0}^{m-1} \sum_{v=0}^{n-1} \hat{\mathbf{X}}_u(u, v) e^{i2\pi(\frac{ux}{m} + \frac{vy}{n})}. \quad (6)$$

Note that Eqs. (5) and (6) are dual, except for an extra normalized coefficient $\frac{1}{mn}$ in the inverse transform. It can be seen that every sampling point in k -space contains the global information of an MR image in the image domain. Likewise, each pixel in an MR image is generated by using all k -space data. Eqs. (5) and (6) can be simplified by using the matrix form:

$$\mathbf{F}_n = \begin{bmatrix} 1 & 1 & 1 & \dots & 1 \\ 1 & \omega & \omega^2 & \dots & \omega^{n-1} \\ \vdots & \vdots & \vdots & \ddots & \vdots \\ 1 & \omega^{n-1} & \omega^{2(n-1)} & \dots & \omega^{(n-1)(n-1)} \end{bmatrix}, \quad (7)$$

$$\omega = \exp(-i2\pi/n), \quad (8)$$

$$\hat{\mathbf{X}}_u = \mathbf{F}_m \mathbf{X}_u \mathbf{F}_n, \quad (9)$$

$$\mathbf{X}_u = \mathbf{F}_m^{-1} \hat{\mathbf{X}}_u \mathbf{F}_n^{-1} = \frac{1}{mn} \mathbf{F}_m^H \hat{\mathbf{X}}_u \mathbf{F}_n^H, \quad (10)$$

where \mathbf{F}_n is the Fourier matrix and $(\cdot)^H$ denotes the Hermitian transpose. Since the dimension of the Fourier matrix can be preset, \mathbf{F}_m and \mathbf{F}_n are computed in advance and not involved in training. Thus, they are considered as constants and are not required to update. The gradient with respect to the input of the inverse Fourier transform can be expressed as

$$\frac{\partial}{\partial \hat{\mathbf{X}}_u} = \frac{\partial}{\partial \mathbf{X}_u} \frac{\partial \mathbf{X}_u}{\partial \hat{\mathbf{X}}_u} = \frac{1}{mn} \mathbf{F}_m^H \frac{\partial}{\partial \mathbf{X}_u} \mathbf{F}_n^H. \quad (11)$$

Hence, the proposed 2D inverse Fourier transform layer adds a little computational cost. Since we have separated the real and imaginary parts in k -space, we can avoid the complex numbers by saving the real and imaginary components of \mathbf{F}_m and \mathbf{F}_n respectively, to accelerate the training period. According to the Euler formula, we obtain

$$\mathbf{F}_n^{\cos} = \begin{bmatrix} 1 & 1 & 1 & \dots & 1 \\ 1 & \eta & \eta^2 & \dots & \eta^{n-1} \\ \vdots & \vdots & \vdots & \ddots & \vdots \\ 1 & \eta^{n-1} & \eta^{2(n-1)} & \dots & \eta^{(n-1)(n-1)} \end{bmatrix}, \quad (12)$$

$$\mathbf{F}_n^{\sin} = \begin{bmatrix} 1 & 1 & 1 & \dots & 1 \\ 1 & \kappa & \kappa^2 & \dots & \kappa^{n-1} \\ \vdots & \vdots & \vdots & \ddots & \vdots \\ 1 & \kappa^{n-1} & \kappa^{2(n-1)} & \dots & \kappa^{(n-1)(n-1)} \end{bmatrix}, \quad (13)$$

$$\eta = \cos(2\pi n), \quad \kappa = -\sin(2\pi n). \quad (14)$$

C. Reconstruction Network

Fig. 3 illustrates the structure of our proposed reconstruction network (RecNet). It is placed after the inverse Fourier trans-

form layer. In this paper, we adopt a common CNN structure with a global skip connection:

$$\mathbf{X}_{\text{rec}} = \mathbf{X}_u + f_{\text{cnn}}(\mathbf{X}_u | \theta), \quad (15)$$

where the depth of CNN is 10, Section V-C explains how we choose the depth. Except the last convolutional layer (kernel 1×1 , channel = 1, stride = 1, pad = 0) for feature fusion, other convolutional layers have the setting of kernel 3×3 , channel = 16, stride = 1, and pad = 0, followed by the rectified linear unit (ReLU) activation to keep nonlinear capability. To achieve the residual learning scheme, the output of RecNet is summed by its input, so that the gradient vanishing problem can be alleviated. Since the main purpose of this paper is learning the 2D probabilistic undersampling pattern, we do not discuss the structural design of the RecNet in detail. After training, the output of RecNet \mathbf{X}_{rec} can approximate the ground-truth MR image \mathbf{Y}_{rec} . To obtain the universal results of sampling matrices, we adopt the traditional Euclidean loss to train our model, defined as the reconstruction loss:

$$L_{\text{rec}} = \frac{1}{2} \|\mathbf{X}_{\text{rec}} - \mathbf{Y}_{\text{rec}}\|_F^2, \quad (16)$$

where $\|\cdot\|_F$ denotes the Frobenius norm.

Unlike other deep learning based MRI reconstruction methods (Fig. 1), we focus on discovering and analyzing the undersampling pattern, rather than designing complicated CNN structures. In Section V-C, we prove that the most efficient way to improve the quality of MR images is optimizing the undersampling pattern in k -space, which is more effective than training large-scale models in the image domain.

IV. IMPLEMENTATION DETAILS

A. Solution to Non-differentiable Undersampling Patterns

Since the values in sampling matrix \mathbf{M}_u are binary, they are non-differentiable (no gradient) and cannot directly take part in backpropagation. Thus, we make full use of the property that sampling matrix \mathbf{M}_u obeys the Bernoulli distribution with probability matrix \mathbf{P}_u , and propose the probabilistic mask auto-training (PMAT) strategy: \mathbf{M}_u is the mask, and \mathbf{P}_u is the probability. Specifically, in each iteration, the forward pass uses the mask \mathbf{M}_u , which is generated by the Bernoulli distribution with probability \mathbf{P}_u . To compute the gradient in backpropagation, \mathbf{P}_u having continuous values from [0, 1] is adopted. These two steps are alternating until probability \mathbf{P}_u converges. As shown in Eqs. (17)–(19) and Fig. 4, our PMAT strategy preserves the probability distribution of sampling matrix \mathbf{M}_u and introduces enough randomness in optimization, so that probability matrix \mathbf{P}_u can be fully trained and is prone to learning underlying patterns. After training, the final result of \mathbf{M}_u from our cross-domain model is the 2D undersampling pattern.

$$\hat{\mathbf{X}}_u = \hat{\mathbf{X}}_{\text{in}} \circ \mathbf{M}_u, \quad (17)$$

$$\frac{\partial}{\partial \mathbf{M}_u} = \frac{\partial}{\partial \hat{\mathbf{X}}_u} \frac{\partial \hat{\mathbf{X}}_u}{\partial \mathbf{M}_u} \approx \frac{\partial}{\partial \hat{\mathbf{X}}_u} \frac{\partial \hat{\mathbf{X}}_u}{\partial \mathbf{P}_u}, \quad (18)$$

$$\frac{\partial}{\partial \hat{\mathbf{X}}_{\text{in}}} = \frac{\partial}{\partial \hat{\mathbf{X}}_u} \frac{\partial \hat{\mathbf{X}}_u}{\partial \hat{\mathbf{X}}_{\text{in}}} = \frac{\partial}{\partial \hat{\mathbf{X}}_u} \mathbf{M}_u \approx \frac{\partial}{\partial \hat{\mathbf{X}}_u} \mathbf{P}_u. \quad (19)$$

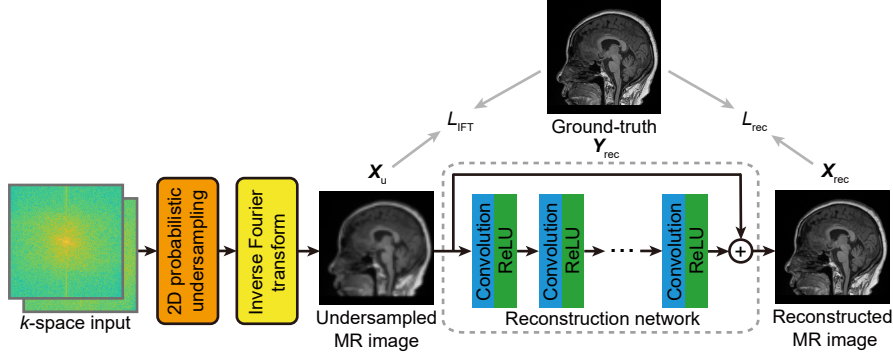


Fig. 3. Overall structure of our proposed cross-domain network: 2D probabilistic undersampling layer, inverse Fourier transform layer, and reconstruction network. L_{IFT} and L_{rec} are combined for training

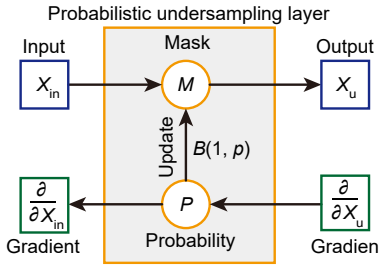


Fig. 4. Forward pass and backpropagation of our 2D probabilistic undersampling layer

Since our proposed PMAT strategy changes the gradient flow during training and current main-stream deep learning frameworks cannot support it, we need to design our custom function. At first, all values of the probability matrix are equal to the preset sampling rate, i.e., $P_u = \text{rate}$, e.g. 10% or 20%. The initial status of sampling matrix M_u is generated by using the Bernoulli distribution with probability matrix P_u . After a number of iterations, P_u will be quite stable, and M_u will be the corresponding undersampling pattern.

Different from those methods [31]–[34], our PMAT strategy can overcome the non-differentiable sampling problem and can adopt real binary masks in optimization. We only need to set a fixed sampling rate and start from a random initial status, instead of complicated initialization. In addition, we can directly obtain the probability matrix for theoretical analysis.

B. Multi-loss Cross-Domain Training

To obtain the universal optimized probability matrix P_u and sampling matrix M_u , we propose an extra Euclidean loss function, after the inverse Fourier transform layer, which is defined as the undersampling loss:

$$L_{\text{IFT}} = \frac{1}{2} \|X_u - Y_{\text{rec}}\|_F^2. \quad (20)$$

This is regarded as an extra constraint for undersampled MR images in training. As shown in Fig. 3, combined with the reconstruction loss L_{rec} , we have the following joint loss function:

$$L_{\text{joint}} = \frac{\lambda_1 \cdot L_{\text{IFT}} + \lambda_2 \cdot L_{\text{rec}}}{\lambda_1 + \lambda_2}, \quad \lambda_1, \lambda_2 \in [0, 1], \quad (21)$$

where λ_1 and λ_2 trade off the importance of two losses. If $\lambda_1 = 0$, it means that L_{IFT} is not used in training [34]. In our experiments, we find that the supervised information is insufficient, and no obvious pattern occurs in the probability matrix or the sampling matrix. If $\lambda_2 = 0$, it means that the RecNet is not involved in training, our model only optimizes the probabilistic undersampling layer to recover MR images. This leads to low-quality results, but saves numerous parameters and much of computational cost.

In this paper, we consider that L_{IFT} and L_{rec} are of equal importance. Thus, our cross-domain model can use L_{IFT} only ($\lambda_1 = 1, \lambda_2 = 0$) to quickly analyze undersampling patterns after optimization; or it can use L_{joint} ($\lambda_1 = 1, \lambda_2 = 1$) to simultaneously train the probabilistic undersampling layer and the RecNet. After training, our sampling matrix M_u and the RecNet are matched together to recover high-quality MR images, while probability matrix P_u can be used for theoretical analysis.

C. Stable Constraints for Undersampling Patterns

Since we use probability matrix P_u to generate sampling matrix M_u by the Bernoulli distribution, to introduce significant randomness. This helps probability matrix P_u to be fully trained. After training, we require stable sampling matrix M_u generated by probability matrix P_u to analyze its pattern. However, randomness will interfere this stage. As shown in Fig. 5a, sampling matrix M_u is generated by probability matrix $P_u = 10\%$ with Bernoulli distribution. It can be seen that those sampling points are randomly placed, where some areas are sparse but others are dense. This makes sampling matrix M_u unstable and difficult to reproduce. Every M_u generated by the same P_u is quite different from each other, so that the performance of the RecNet varies intensely. This apparently prevents probability matrix P_u from convergence.

According to the definitions in physics, the distance between gas molecules changes drastically, similar to Fig. 5a; however, the distance between solid molecules is relatively fixed, similar to Fig. 5b. Hence, to overcome the interference caused by randomness, we propose the following stable constraints, applied in the stage when probability matrix P_u generates sampling matrix M_u ($P_u \rightarrow M_u$):

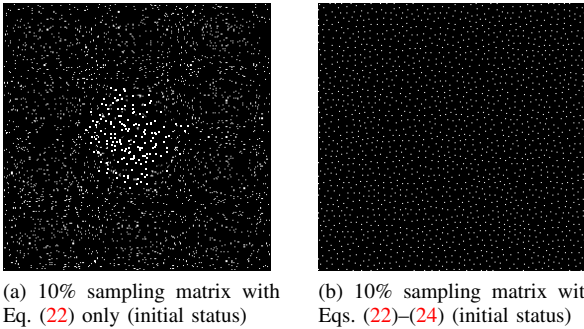


Fig. 5. 10% sampling matrices with two constraints respectively

- 1) **Total sampling rate constraint.** During training, the average of probability matrix \mathbf{P}_u should equal the preset sampling rate. Since all experiments in this paper are based on the fixed sampling rate, Eq. (22) is considered as an essential constraint.

$$\|\bar{\mathbf{P}}_u - \text{rate}\|_2 < \epsilon. \quad (22)$$

- 2) **Regional sampling distance constraint.** In each region $\mathcal{C} \in \mathbb{R}^{10 \times 10}$, the number of sampling points is allocated according to its probability, i.e., the larger the probability is, the more the sampling points will be. The distance between those sampling points with the same probability should be nearly uniform, ranging from $[r_0, 2r_0]$. Eqs. (23) and (24) can apparently influence the final pattern in \mathbf{M}_u .

$$\left\| \bar{p} - \frac{\sum_{x,y \in \mathcal{C}} |\mathbf{M}_u(x,y)|}{mn} \right\|_2 < \epsilon. \quad (23)$$

$$r_0 < \|\mathbf{M}_u(x_i, y_j) - \mathbf{M}_u(x_k, y_l)\|_2 < 2r_0, \quad (24)$$

$$\forall i, k = 1, 2, \dots, m, \quad \forall j, l = 1, 2, \dots, n. \quad (25)$$

Here, $\epsilon = 0.1\%$ is the tolerance, which makes sure that the difference between the actual sampling rate and the preset value is smaller than 0.1%. $\bar{\mathbf{P}}_u$ denotes the average of the probability matrix. \bar{p} denotes the actual average of region $\mathcal{C} \in \mathbb{R}^{10 \times 10}$. r_0 denotes the preset minimal distance of all sampling points. According to the curve fitting results, we obtain $\bar{p} = \frac{\sqrt{2}}{10} r_0^2 - \frac{\sqrt{2}}{2} r_0 + 1.0$. Since the actual sampling distance is integer, distributing sampling points in \mathbf{M}_u will bring in a little localization error. But we confirm this error is negligible by rigorously assuring $\|\bar{\mathbf{P}}_u - \text{rate}\|_2 < \epsilon$.

Our stable constraints include two parts: 1) (essential) total sampling rate constraint (22); 2) (optional) regional sampling distance constraint (23) and (24). They are applied in the stage when probability matrix \mathbf{P}_u generates sampling matrix \mathbf{M}_u . As shown in Fig. 4, this stage is not involved in the gradient calculation. Thus, when training, the processes of $\mathbf{P}_u \rightarrow \mathbf{M}_u$, forward pass, and backpropagation are alternately carried out. As shown in Fig. 5b, with constraints (22)–(24), sampling matrix \mathbf{M}_u is generated by probability matrix $\mathbf{P}_u = 10\%$. It reveals that all sampling points in \mathbf{M}_u are uniformly distributed, where no sparse or dense area exists. Furthermore, with the stable constraints, the sampling matrix is quite easy to reproduce, and its corresponding pattern is

obvious. Section V-D will demonstrate the effect of these stable constraints.

D. Training Configurations and Initialization

At the initial stage of the 2D probabilistic undersampling layer, all values in probability matrix \mathbf{P}_u are equal to the target sampling rate, i.e., $\mathbf{P}_u = 10\%$ or 20% . Eq. (22) (i.e., $\bar{\mathbf{P}}_u \approx \text{rate}$) is guaranteed during training. The initial status of sampling matrix \mathbf{M}_u is decided by probability matrix \mathbf{P}_u with Bernoulli distribution. As the training progresses, \mathbf{M}_u will be stable when \mathbf{P}_u converges. Since each value of probability matrix \mathbf{P}_u follows $p \in [0, 1]$, we propose an upper bound $p \leq P_{\max} = 1$, in case that the probability overflows. In addition, the Bernoulli distribution makes no sense when $p = 0$, causing the corresponding values in sampling matrix \mathbf{M}_u cannot be updated. This leads to a local minimum and poor performance of the RecNet. To this end, we propose a lower bound $p \geq P_{\min}$. Together with the total sampling rate constraint (22), Section V-F will demonstrate how to decide the precise value of P_{\min} .

Since no trainable parameter exists in the inverse Fourier transform layer, we only need to preserve the Fourier matrices of Eqs. (12) and (13) during initialization.

Our cross-domain model is trained respectively in two situations: 1) using L_{IFT} ($\lambda_1 = 1, \lambda_2 = 0$) and 2) using L_{joint} ($\lambda_1 = \lambda_2 = 1$), to analyze the undersampling patterns and compare the quality of MR images.

The training configurations of our model are summarized in Table I. We set the initial learning rate as 10^{-3} , which will be divided by $\sqrt{10}$ in every 20 epochs, until it reaches the minimum 10^{-8} . We use the Adam [36] optimizer with default coefficients $\beta_1 = 0.9$ and $\beta_2 = 0.999$. In addition, we adopt the early-stopping strategy: the training will terminate in advance if no improvement occurs in 15 successive epochs. Some settings of the RecNet have been given in Section III-C. To keep the dimensions of input and output identical, we adopt the zero-padding scheme in each convolutional layer. We set the depth of the RecNet as 10, denoted as RecNet-10. Section V-C will demonstrate how we select the depth of the RecNet.

TABLE I
TRAINING CONFIGURATIONS OF OUR CROSS-DOMAIN MODEL

Description	Value		Description	Value
Batch	16		Optimizer	Adam [36]
Maximal epoch	200		β_1 of Adam	0.9
Initial learning rate	1e-3		β_2 of Adam	0.999
Learning policy	Stair-case		Minimal learning rate	1e-8
Learning decay	$\sqrt{10}$		Weight decay	1e-5
Decay step	20		Device	GPU

V. EXPERIMENTS

Our source code is available online³. It is based on Tensorflow [37] with Keras APIs. Our experiments are executed on a Ubuntu Linux server, equipped with an Intel Xeon(R)

³<https://github.com/xueshengke/2D-PUPO>

Platinum CPU @ 2.50 GHz, total 528 GB memory, and four NVIDIA Tesla V100 (32 GB) GPUs. Our 2D probabilistic undersampling strategy is compared with several existing undersampling methods under sampling rates 10%–50%. The compared methods are J-CUR [34] (Fig. 6a), PFGMS [31] (Fig. 6b), J-MoDL [33] (Fig. 6c), LOUP [35] (Fig. 6d), Gaussian sampling [38] (Fig. 6e), and Poisson sampling [39] (Fig. 6f). For fair comparison, we replace our probability and sampling matrices with those compared (either learned or fixed) patterns, then train our cross-domain model. As the model parameters trained under different undersampling cases cannot be shared, we train multiple models individually for various sampling rates.

In addition, the main focus of this paper is to optimize the undersampling pattern and to discover the optimal probability distribution, through our 2D probabilistic undersampling layer, rather than designing complicated CNN structures. Consequently, we do not conduct the architecture search for the RecNet. Section V-D will prove that the quality of recovered MR images is improved mainly by the learned 2D probabilistic undersampling pattern, secondly by the trained RecNet.

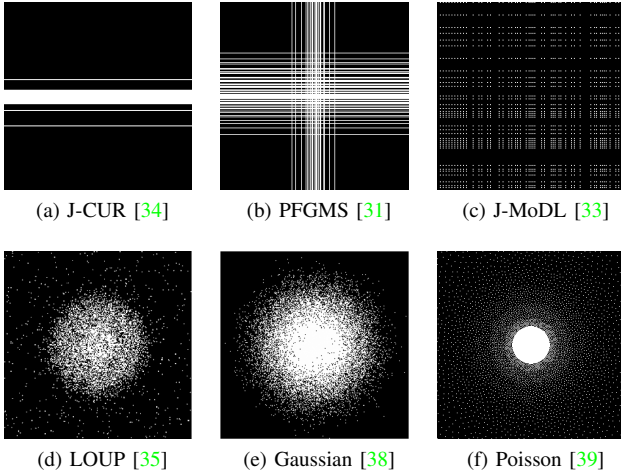


Fig. 6. Several existing k -space undersampling patterns

A. Datasets

We adopt the 3T brain MR images from Multi-modal Brain Tumor Segmentation Challenge 2018 [40], [41], as the training and validation sets, denoted as BraTS 2018. All image slices are obtained by 3D scanning and saved in the NIfTI format. Specifically, it contains 200 training volumes and 50 validation volumes. Each volume comes from one patient/candidate. The spatial resolution is $256 \times 256 \times (240\text{--}320)$, the minimal voxel is $1 \text{ mm} \times 1 \text{ mm} \times 1 \text{ mm}$. We choose 200 volumes for training, 10 out of 50 volumes for validation. All pixels are normalized to $[0, 1]$.

To verify the performance of our method, we adopt the brain 3T/7T, T1/T2 modals, 3D scanning, fully-sampled k -space data and MR images of volunteers (acquired by a SIEMENS Prisma MRI scanner) as the test set, denoted as Test3T&7T. It consists of 20 volumes of k -space data from 20 different volunteers, each of which contains 192 image slices. The

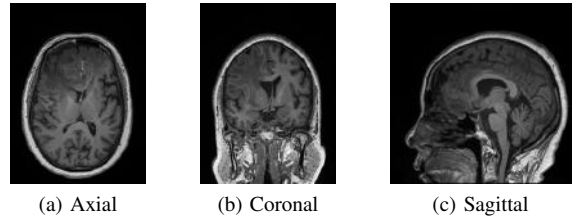


Fig. 7. An example of brain MR images from Test3T&7T

spatial resolution is $256 \times 256 \times 192$, and the minimal voxel is $0.9375 \text{ mm} \times 0.9375 \text{ mm} \times 1 \text{ mm}$. Fig. 7 shows the an example of Test3T&7T.

Since we focus only on the human tissue and ignore the background in MR images, we propose the following data augmentation strategy:

- 1) **Translation.** All contents of tissue are translated to the geometrical center of MR images.
- 2) **Rotation.** All images are randomly rotated $[0, 360]$ degrees by 8 times.

This strategy is used to prevent the over-fitting problem and boost the generalization capability of our model. Because most of images in BraTS 2018 are similar and have fixed shapes, except for small difference from various samples, the diversity of k -space data is not enough. To obtain the universal probabilistic undersampling patterns after training, our data augmentation strategy (translation and random rotation) significantly enriches the diversity of our training set. Section V-F shows that our probability matrices trained under various sampling rates are perfectly symmetric.

To keep the dimension of training data consistent, we concatenate all MR images along the sagittal direction. Thus, during training and validation, the dimension of one batch becomes $256 \times 256 \times N$, where N is the batch size.

In our model, we adopt two loss functions: undersampling loss L_{IFT} and reconstruction loss L_{rec} , for supervised training. Correspondingly, we present two indicators: undersampling PSNR and reconstruction PSNR for comparison.

Since the k -space data are used as the input of our model while BraTS 2018 only provides MR images, we need to convert all training and validation images into the frequency domain via the 2D fast Fourier transform. As for the test set, we directly use 3T/7T fully-sampled k -space data. To avoid complex values, we split the real and imaginary parts, then combine them as two channels. Since the purpose of our method is reconstruction, the MR images in training and test sets naturally can be used as the ground-truth.

B. Evaluation Metric

Peak signal-to-noise ratio (PSNR) has been commonly used to measure the quality of MR images in various computer vision tasks. PSNR is defined as follows:

$$\text{MSE} = \frac{1}{N} \| \mathbf{I}_{\text{rec}} - \mathbf{I}_{\text{gnd}} \|_{\text{F}}^2, \quad (26)$$

$$\text{PSNR} = 10 \cdot \log_{10} \left(\frac{P_{\text{max}}^2}{\text{MSE}} \right) \text{ dB}, \quad (27)$$

where I_{rec} is the recovered image, I_{gnd} is the original image, and P_{\max} is the maximum pixel value (normally 1.0) of an image. A high-quality MR image usually has a large value of PSNR. Structural similarity index (SSIM) [42] is often adopted to evaluate the quality of MR images. However, we find that in most cases, the values of SSIM of recovered MR images are nearly equal to 1.0, which are very difficult to distinguish. Thus, in this paper, we use only PSNR as the effective metric to evaluate the performances of different methods.

C. Effect of Reconstruction Network

Table II shows the PSNR of our 2D probabilistic undersampling layer with different depths of RecNet, based on Test3T&7T set, under sampling rate 10%–50%. It can be seen that the difference between the actual sampling rate and the target value is quite small (<0.1%), which proves the effectiveness of our total sampling rate constraint (22). As the sampling rate or the depth of RecNet increases, the undersampling PSNR and reconstruction PSNR both improve significantly. Note that the improvement mainly comes from our 2D probabilistic undersampling patterns, then from our trained RecNet. The deeper the RecNet is, the better the quality of MR images we can obtain. In addition, when the sampling rates are identical, the undersampling PSNR also improves with the increasing of the depth of RecNet, which indicates that our cross-domain training scheme can simultaneously optimize the 2D probabilistic undersampling layer and the RecNet, and obtain matched sampling matrices and parameters of RecNet.

Fig. 8 shows the number of parameters, Flops, and memory of our 2D probabilistic undersampling layer with different depths of RecNet, based on BraTS 2018 training set. Most parameters are in the probability matrix and sampling matrix of our 2D probabilistic undersampling layer, i.e., $256 \times 256 \times 2 = 131,072$. In the RecNet, only a few parameters exist. However, as the depth of RecNet increases, the number of Flops rises rapidly, because the feature maps with the size of 256×256 require a huge amount of computational cost in convolution. Likewise, the memory consumption is proportional to the depth of RecNet during training. To balance the performance and computational burden of our model, we choose the depth as 10 in the rest of experiments.

D. Effect of Stable Constraints

Fig. 9 shows the sampling matrices of our 2D probabilistic undersampling layer, under sampling rate 10.05% and 30.01% with Eq. (22) and Eqs. (22)–(24), respectively. As shown in Figs. 9a and 9b, the sampling points in k -space are distributed randomly since no regional sampling distance constraints (23) and (24) are used. Especially in the HF area, those sampling points generated by the Bernoulli distribution are either too sparse or too dense, though their probability values are the same. This apparently prevents us from analyzing its probability distribution. As shown in Figs. 9c and 9d, those sampling points in k -space are uniformly distributed by adopting (23) and (24), especially in the HF area. This intuitively indicates that the probability values are equal in that area. In addition,

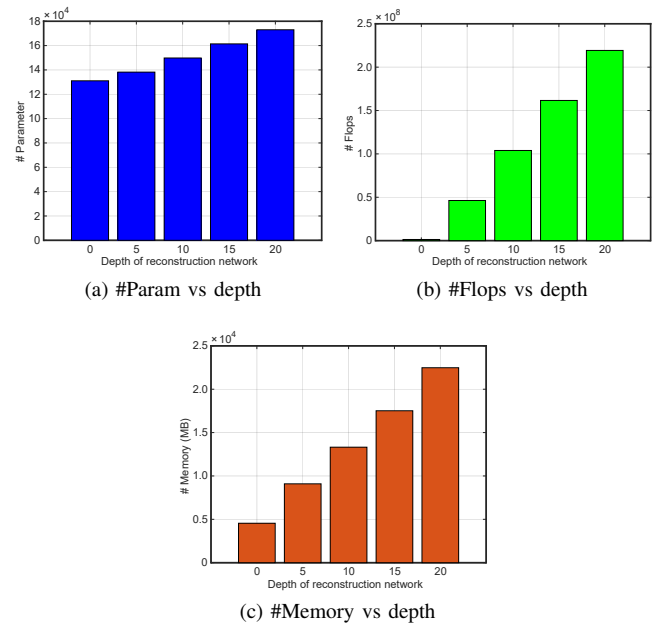


Fig. 8. #Param, #Flops, and #Memory of our 2D probabilistic undersampling layer with different depths of RecNet, based on BraTS 2018 training set

after integrating the regional sampling distance constraint, the sampling matrices are quite stable and repeatable even through multiple trials.

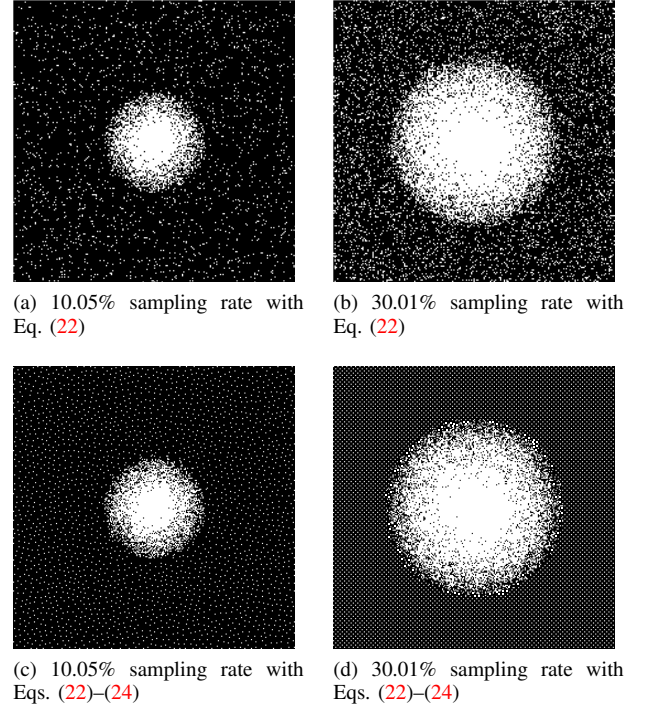


Fig. 9. Sampling matrices of our 2D probabilistic undersampling layer, under sampling rate 10.05% and 30.01% with Eq. (22) and Eqs. (22)–(24), respectively

Fig. 10a shows the PSNR of our 2D probabilistic undersampling layer (no RecNet), by using the total sampling rate constraint and regional sampling distance constraint respectively,

TABLE II
PSNR OF OUR 2D PROBABILISTIC UNDERSAMPLING LAYER WITH DIFFERENT DEPTHS OF RECNET, BASED ON TEST3T&7T SET, UNDER SAMPLING RATE 10%–50%

Sampling rate	Undersampling PSNR (dB) / Reconstruction PSNR (dB)				
	RecNet-0	RecNet-5	RecNet-10	RecNet-15	RecNet-20
10.09%	32.80 / –	33.03 / 36.43	34.25 / 37.34	34.99 / 38.08	35.33 / 38.74
20.01%	34.98 / –	35.67 / 38.49	36.83 / 39.15	36.99 / 39.87	37.68 / 40.09
29.91%	36.06 / –	37.01 / 40.91	38.70 / 41.46	39.04 / 42.34	39.63 / 42.97
40.04%	37.14 / –	39.49 / 41.99	40.99 / 43.87	41.51 / 44.13	42.03 / 44.55
50.00%	39.56 / –	41.32 / 44.56	42.01 / 45.92	42.51 / 46.21	43.36 / 46.36

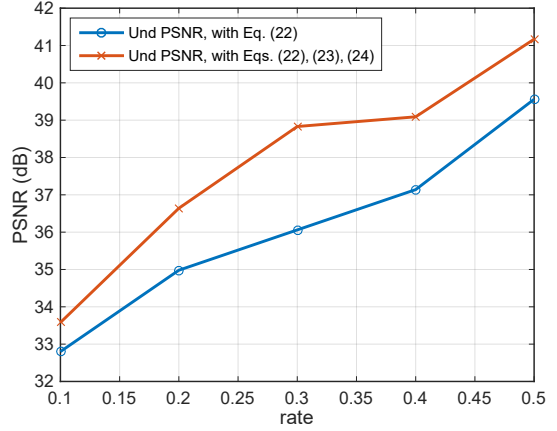
based on Test3T&7T set, under sampling rate 10%–50%. It can be seen that the regional sampling distance constraint not only helps generate stable sampling matrices, but also improves the undersampling PSNR of MR images by nearly 0.8–2.8 dB.

Fig. 10b shows the PSNR of our 2D probabilistic undersampling layer (with RecNet-10), by using the total sampling rate constraint and regional sampling distance constraint respectively, based on Test3T&7T set, under sampling rate 10%–50%. With the advantage of RecNet-10, our method can further improves the PSNR of final MR images by nearly 0.7–2.1 dB. In addition, we discover that the improvement mainly results from the stable sampling matrices. Although RecNet-10 continually increases the values of PSNR, its effect has been quite limited.

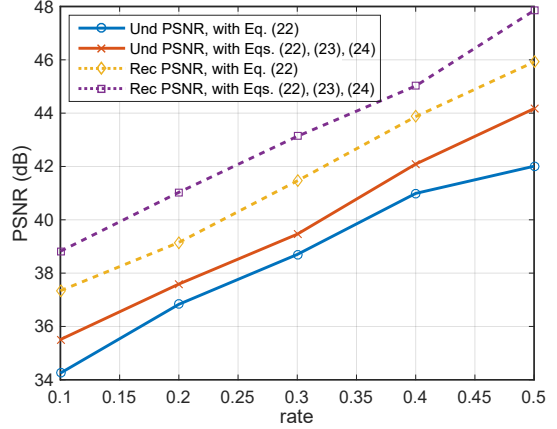
The total sampling rate constraint ensures that the difference between the actual sampling rate and the target value is smaller than 0.1%. This is convenient for us to analyze the relationship between the sampling matrix and the sampling rate. Besides, in the rest of experiments, we adopt the total sampling rate constraint and regional sampling distance constraint together (known as stable constraints), to obtain stable sampling matrices and substantially improve the PSNR of final MR images.

E. Comparison of Different Undersampling Patterns

Table III compares the PSNR values from different undersampling methods (with RecNet-10) based on Test3T&7T set, under sampling rate 10%–50%. As the sampling rate increases, the PSNR values of all methods improve gradually. It can be seen that the undersampling patterns of J-CUR and PFGMS perform worse than others, where the J-CUR only samples in 1D phase encoding direction and ignores the other dimension, as shown in Fig. 6a. Since PFGMS allocates most sampling lines in the LF area, as shown in Fig. 6b, its PSNR value is slightly better than J-CUR. Their common disadvantage is that the majority of HF information is lost, leading to low-quality of MR images. J-MoDL trains both the deep network and 2D undersampling pattern, but it samples evenly in the LF and HF areas, as shown in Fig. 6c, so that its PSNR value is within 2.3 dB better than two methods mentioned above. This indicates that the improvement of the undersampling pattern by J-MoDL is still limited. However, the undersampling pattern of LOUP, which is symmetric in Fig. 6d, properly allocates the sampling points in LF and HF areas. Thus, it obviously improves the PSNR of recovered images. In addition, by using 2D probability functions, Gaussian and Poisson undersampling



(a) Undersampling PSNR, no RecNet



(b) Undersampling / Reconstruction PSNR, with RecNet-10

Fig. 10. PSNR of our 2D probabilistic undersampling layer, by using the total sampling rate constraint and regional sampling distance constraint respectively, based on Test3T&7T set, under sampling rate 10%–50%

patterns have similar PSNR values and both outperform aforementioned methods. As a result, our proposed probabilistic undersampling pattern, integrated with RecNet-10, can obtain 2–3 dB higher values of PSNR than Gaussian and Poisson undersampling methods, under various sampling rates. Unlike other sampling patterns, our probability matrix can accurately control the (i.i.d) status of every sampling points, and our sampling matrix only requires random initialization. By jointly cross-domain training the undersampling pattern and RecNet, our method can effectively obtain the best PSNR of recovered MR images.

TABLE III
COMPARISON OF PSNR FROM DIFFERENT UNDERSAMPLING METHODS (WITH RECNET-10) BASED ON TEST3T&7T SET, UNDER SAMPLING RATE 10%–50%

Sampling rate	Undersampling PSNR (dB) / Reconstruction PSNR (dB)						
	J-CUR [34]	PFGMS [31]	J-MoDL [33]	LOUP [35]	Gaussian [38]	Poisson [39]	Probabilistic
10.09%	27.23 / 30.85	29.51 / 31.02	30.19 / 33.35	31.48 / 34.21	33.08 / 36.34	33.21 / 36.95	35.51 / 38.2
20.01%	29.46 / 31.34	31.35 / 33.24	32.37 / 35.08	33.76 / 36.85	35.39 / 39.30	35.26 / 39.13	37.59 / 41.03
29.91%	30.54 / 32.83	32.48 / 35.91	33.89 / 36.72	35.30 / 38.76	37.27 / 41.06	37.53 / 41.44	39.46 / 43.13
40.04%	31.09 / 33.15	33.72 / 37.67	35.64 / 38.28	37.49 / 39.97	39.31 / 41.83	39.22 / 42.00	42.09 / 45.02
50.00%	32.64 / 34.79	35.83 / 39.67	37.28 / 39.96	38.65 / 41.40	40.20 / 43.15	40.42 / 43.66	44.17 / 47.85

Fig. 11 compares the recovered MR images from different undersampling methods (with RecNet-10) based on Test7T set, under sampling rate 20%. It can be seen that the recovered MR images by the J-CUR and PFGMS methods are quite blurry, and some details have been lost in the undersampling process. By increasing the sampling rate in the HF area, J-MoDL method obviously improves the PSNR of final results. However, its improvement is fairly limited, because J-MoDL deals with the LF and HF areas evenly, by allocating nearly identical sampling rates. In contrast, the LOUP method has most sampling points in the LF area and keeps a small number of sampling points randomly in the HF area, which apparently reconstructs some tiny details in MR images. In addition, by generating from 2D probability functions, the Gaussian and Poisson undersampling methods accurately distribute every sampling point in k -space, which significantly reconstructs sophisticated structures and improves the quality of MR images. Our proposed 2D probabilistic undersampling pattern, trained with RecNet-10 by fully-sampled k -space data, distributes those sampling points in LF and HF areas by using the i.i.d probability values. Thus, our method can effectively obtain higher PSNR values of MR images. Besides, we find that the improvement of PSNR mainly comes from our probabilistic undersampling pattern, which efficiently selects crucial data in k -space. After the undersampling process, RecNet-10 is then adopted to further improve the quality of MR images.

F. Analysis of 2D Probabilistic Undersampling Pattern

Fig. 12 shows the probability matrices and sampling matrices from our 2D probabilistic undersampling layer (no RecNet), trained with the undersampling loss and stable constraints, under the sampling rates 10%–40%. As we can see, the probability values in the central area of the probability matrix are the largest and highly symmetric, while all probability values in the HF area are equal to P_{\min} . Since we have adopted the translation and random angle rotation strategy to effectively overcome the drawback by the insufficient diversity of MR images, our final probability matrices reveal the perfect concentric circle shape. As mentioned earlier, our final probability matrix can also be considered as the importance distribution of sampling points in k -space, where the LF area is used to obtain the overall structure of MR images and the HF area is crucial to recover the sophisticated details in MR images. As the total sampling rate increases, the central circle area enlarges and the minimal probability value (i.e. P_{\min}) also rises. From the sampling matrices in Fig. 12, we

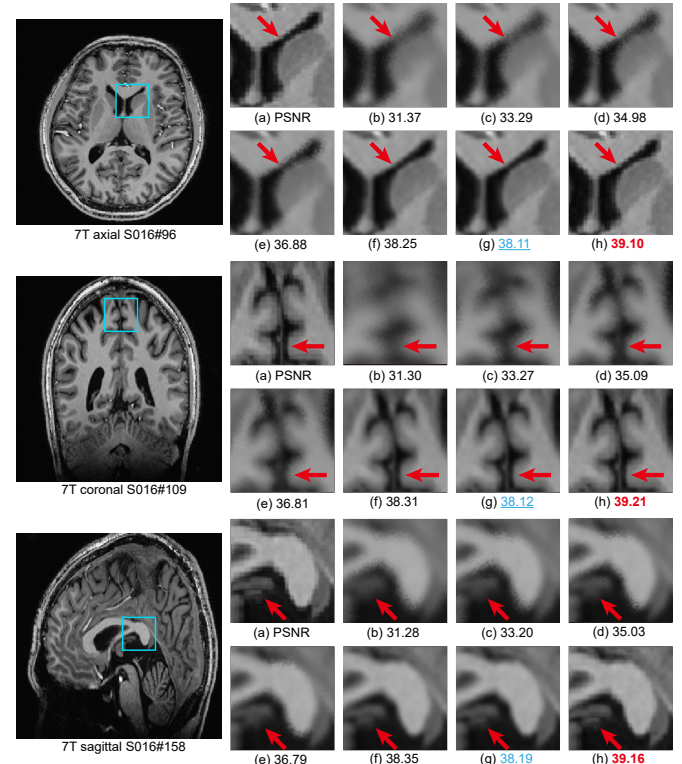


Fig. 11. Comparison of recovered MR images from different undersampling methods (with RecNet-10) based on Test7T set, under sampling rate 20%: (a) Original; (b) J-CUR; (c) PFGMS; (d) J-MoDL; (e) LOUP; (f) Gaussian; (g) Poisson; (h) Probabilistic

find that the sampling points in the LF area are pretty dense, while they are fairly sparse in the HF area. In addition, all sampling points are uniformly distributed in Fig. 12, which proves the effectiveness of integrating the stable constraints when generating the sampling matrix M_u .

Because the probability matrices (Fig. 12) comprise special patterns, we continue to precisely analyze: the 3D probability curve P_{face} , central probability curve P_{center} , and marginal probability curve P_{margin} , as shown in Fig. 13. As the total sampling rate increases, the probability values in the LF area are much closer to 1.0, and the minimal probability value P_{\min} is higher. In addition, since the probability matrices are quite symmetric, the curves in row and column directions of P_{center} (or P_{margin}) are identical. Thus, in our experiments, we only need to focus on one direction for analysis. The maximal value of P_{center} is 1.0, and its minimal value is P_{\min} . With the

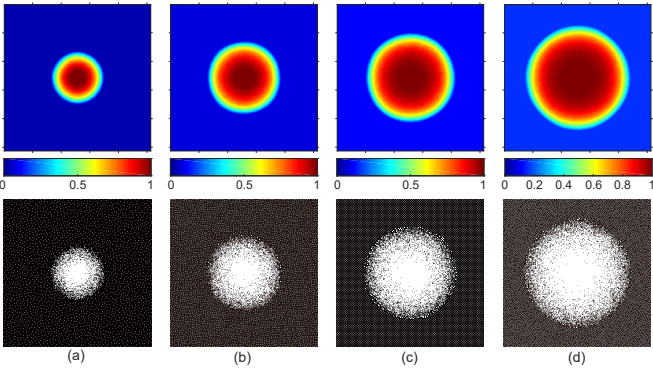


Fig. 12. Probability matrices and sampling matrices from our 2D probabilistic undersampling layer (no RecNet), trained with the undersampling loss and stable constraints. Sampling rate: (a) 10%; (b) 20%; (c) 30%; (d) 40%

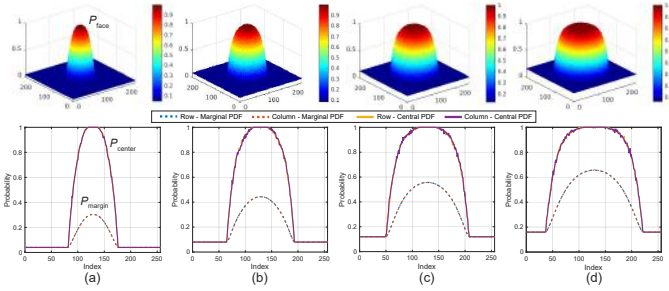


Fig. 13. Curves of the probability matrices from 2D probabilistic undersampling layer: 3D probability curve P_{center} , central probability curve P_{center} , and marginal probability curve P_{margin} . Sampling rate: (a) 10%; (b) 20%; (c) 30%; (d) 40%

increasing of total sampling rate, P_{center} becomes wider, and P_{margin} becomes both higher and wider.

According to the curves in Fig. 13, we assume that P_{center} and P_{margin} both satisfy specific functions, and are inherently proportional to the total sampling rate. By exploiting the curve fitting tools (Fig. 14), we discover the matched function types for P_{center} and P_{margin} respectively:

$$P_{\text{center}}(t) = \begin{cases} 1, & |t| \leq t_1, \\ c_0 - a_0 e^{b_0(t-t_1)}, & t_1 < |t| < t_0, \\ P_{\min}, & t_0 \leq |t| \leq 1, \end{cases} \quad (28)$$

$$P_{\text{margin}}(t) = \begin{cases} -a_1 t^2 + b_1 t + c_1, & |t| < t_0, \\ P_{\min}, & t_0 \leq |t| \leq 1, \end{cases} \quad (29)$$

$$t = \frac{z - 128}{128} \in [-1, 1], \quad z = 0, 1, 2, \dots, 256, \quad (30)$$

where t is normalized to $[-1, 1]$, and coefficients $\{a_0, b_0, c_0\}$, $\{a_1, b_1, c_1\}$, and $\{t_0, t_1, P_{\min}\}$ are required to take part in the curve fitting process. Table IV summarizes the results of some coefficients under different sampling rates. As shown in Fig. 15, by fitting the data from Table IV, we obtain the relationship between those coefficients and the total sampling rate:

$$a_0 = \frac{1}{100\sqrt{\text{rate}}}, \quad b_0 = \frac{8.1}{\text{rate} + 2/3}, \quad c_0 = P_{\max} = 1, \quad (31)$$

$$a_1 = \frac{\text{rate}}{3\sqrt{2\pi\sigma^4}}, \quad b_1 = 0, \quad c_1 = \frac{2\text{rate}}{\sqrt{2\pi\sigma}}, \quad (32)$$

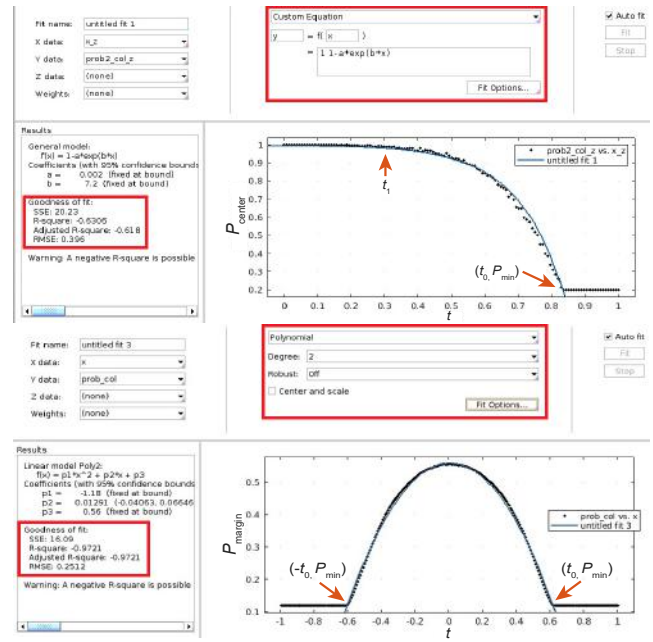


Fig. 14. Curve fitting of the central probability curve P_{center} and marginal probability curve P_{margin}

TABLE IV
CURVE FITTING RESULTS OF THE COEFFICIENTS OF P_{center} AND P_{margin} WITHOUT RECNET, UNDER SAMPLING RATE 10%–50%

Sampling rate	a_0	b_0	c_0	a_1	b_1	c_1
10%	0.0315	10.690	1.001	2.204	0.004	0.303
20%	0.0208	9.308	1.002	1.507	-0.008	0.441
30%	0.0176	8.318	0.998	1.186	0.002	0.562
40%	0.0156	7.563	0.997	0.985	0.006	0.667
50%	0.0132	7.116	0.999	0.821	-0.001	0.754

where σ is an extra coefficient for clear notations. Then to obtain the relationship between coefficients $\{t_0, t_1, P_{\min}\}$ and the total sampling rate, we adopt the integral property of the marginal probability function: in the limited sampling interval, the integral value of the marginal probability function divided by that of the maximum probability is equal to the target total sampling rate. Combining with Figs. 13 and 14, we define the above property as:

$$\frac{S_{\text{margin}}}{S_{\max}} = \text{rate}, \quad (33)$$

$$S_{\max} = \int_{-1}^1 P_{\max} dt = \int_{-1}^1 1 dt = 2, \quad (34)$$

$$S_{\text{margin}} = \int_{-1}^{-t_0} P_{\min} dt + \int_{-t_0}^{t_0} P_{\text{margin}} dt + \int_{t_0}^1 P_{\min} dt = 2 \text{ rate}. \quad (35)$$

By using P_{margin} in Fig. 13, we have the following explanation: with the even symmetry of probability functions, the integral value of the maximal probability $P_{\max} = 1$ in the interval $[-1, 1]$ is equal to 2. Similarly, after training with the target total sampling rate, the joint integral value of P_{margin}

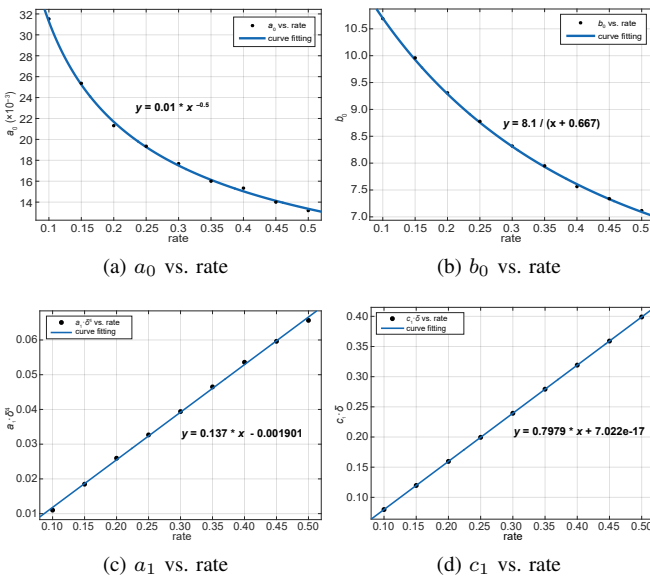


Fig. 15. Curve fitting results of the relationships between a_0, b_0, a_1, c_1 and the total sampling rate

and P_{\min} in the interval $[-1, 1]$ is twice as the sampling rate. By using the even symmetry, we further solve (35) and obtain:

$$2 \int_0^{t_0} P_{\text{margin}} dt + 2 \int_{t_0}^1 P_{\min} dt = 2 \text{rate}, \quad (36)$$

$$\int_0^{t_0} P_{\text{margin}} dt + \int_{t_0}^1 P_{\min} dt = \text{rate}, \quad (37)$$

$$-\frac{1}{3}a_1 t_0^3 + c_1 t_0 + P_{\min}(1 - t_0) = \text{rate}, \quad (38)$$

$$P_{\min} = P_{\text{margin}}(t_0) = -a_1 t_0^2 + c_1, \quad (39)$$

$$-\frac{1}{3}a_1 t_0^3 + c_1 t_0 + (-a_1 t_0^2 + c_1)(1 - t_0) = \text{rate}, \quad (40)$$

$$\frac{2}{3}a_1 t_0^3 - a_1 t_0^2 + c_1 = \text{rate}. \quad (41)$$

By substituting (31), (32) into (41), we have the following:

$$\begin{cases} \frac{2}{3} \cdot \frac{\text{rate}}{3\sqrt{2}\pi\sigma^4} t_0^3 - \frac{\text{rate}}{3\sqrt{2}\pi\sigma^4} t_0^2 + \frac{2\text{rate}}{\sqrt{2}\pi\sigma} = \text{rate}, \\ P_{\text{margin}}(t_0) = P_{\min} = -\frac{\text{rate}}{3\sqrt{2}\pi\sigma^4} t_0^2 + \frac{2\text{rate}}{\sqrt{2}\pi\sigma}, \end{cases} \quad (42)$$

then we obtain the relationship between $\{t_0, t_1, P_{\min}\}$ and the total sampling rate, as shown in Table V. Thus, we conclude the concrete expressions of P_{center} and P_{margin} as:

$$t_0 = \sqrt{6\sigma^3 - 3\sigma^4}, \quad t_1 = \frac{\text{rate}}{\sqrt{2}}, \quad P_{\min} = \frac{\text{rate}}{\sqrt{2}\pi}, \quad (43)$$

$$P_{\text{center}}(t) = \begin{cases} 1, & |t| \leq t_1, \\ 1 - \frac{1}{100\sqrt{\text{rate}}} e^{\frac{8.1}{\text{rate}+2/3}(t-t_1)}, & t_1 < |t| < t_0, \\ \frac{\text{rate}}{\sqrt{2}\pi}, & t_0 \leq |t| \leq 1, \end{cases} \quad (44)$$

$$P_{\text{margin}}(t) = \begin{cases} -\frac{\text{rate}}{3\sqrt{2}\pi\sigma^4} t^2 + \frac{2\text{rate}}{\sqrt{2}\pi\sigma}, & |t| < t_0, \\ \frac{\text{rate}}{\sqrt{2}\pi}, & t_0 \leq |t| \leq 1, \end{cases} \quad (45)$$

$$t = \frac{z - 128}{128} \in [-1, 1], \quad z = 0, 1, 2, \dots, 256. \quad (46)$$

TABLE V
CURVE FITTING RESULTS OF THE COEFFICIENTS OF THE CROSS POINTS OF P_{center} AND P_{margin} WITHOUT RECNET, UNDER SAMPLING RATE 10%–50%

Sampling rate	σ	t_0	t_1	P_{\min}
10%	0.2660	0.3434	0.0709	0.0406
20%	0.3627	0.4867	0.1416	0.0847
30%	0.4274	0.6091	0.2122	0.1223
40%	0.4836	0.7095	0.2830	0.1666
50%	0.5319	0.8202	0.3533	0.1984

Although we have not discovered the relationship between σ and the total sampling rate, we still can obtain the exact expression of P_{center} by training our cross-domain model. Besides, because the probability matrix is highly symmetric in the row and column dimensions, we can directly obtain the expression of P_{face} by extending P_{center} to another dimension:

$$P_{\text{face}}(y, z)$$

$$= \begin{cases} 1, & |d| \leq t_1, \\ 1 - \frac{1}{100\sqrt{\text{rate}}} e^{\frac{8.1}{\text{rate}+2/3}(d-t_1)}, & t_1 < |d| < t_0, \\ \frac{\text{rate}}{\sqrt{2}\pi}, & t_0 \leq |d| \leq \sqrt{2}, \end{cases} \quad (47)$$

$$d = \frac{\sqrt{(y-128)^2 + (z-128)^2}}{128} \in [0, \sqrt{2}], \quad (48)$$

$$\forall y = 0, 1, 2, \dots, 256, \quad \forall z = 0, 1, 2, \dots, 256. \quad (49)$$

Thus, we can accurately obtain the probability value of each sampling point by using (47). Together with Table V, we have proved that our probability function has the following properties:

$$\begin{aligned} \frac{1}{2} \int_{-1}^1 P_{\text{face}}(y, z=0) dy &= \frac{1}{2} \int_{-1}^1 P_{\text{face}}(y=0, z) dz \\ &\approx P_{\text{margin}}(0) = \frac{2\text{rate}}{\sqrt{2\pi}\sigma}, \end{aligned} \quad (50)$$

$$\int_{-1}^1 \int_{-1}^1 P_{\text{face}}(y, z) dy dz \approx 2 \text{rate}, \quad \text{rate} \in [0.1, 0.5]. \quad (51)$$

Finally, we can use (44)–(47) generate different probability matrices and sampling matrices under various sampling rates. Except for the minimal probability limitation $P_{\min} = \frac{\text{rate}}{\sqrt{2}\pi}$, our 2D probabilistic undersampling pattern has no other hyper-parameter. By using our data argumentation strategy, traditional Euclidean loss, and stable constraints, we can obtain optimal undersampling patterns by using a small amount of k -space data. Fig. 16 shows the optimal probability matrix, sampling matrix, and its 3D view under 20% sampling rate, where the patterns in other two directions are also given in Figs. 16e and 16f, respectively.

Though our proposed 2D probabilistic undersampling pattern (Fig. 12) is quite similar to that of LOUP [35] (Fig. 6d), we declare that there are several differences. First, as mentioned in Section II-B, LOUP adopts continuous values by the sigmoid function to approximate the binary values (0/1). Besides, their pattern needs special initialization. Moreover, LOUP does not use stable constrains or provide any theoretical analysis for its undersampling patterns.

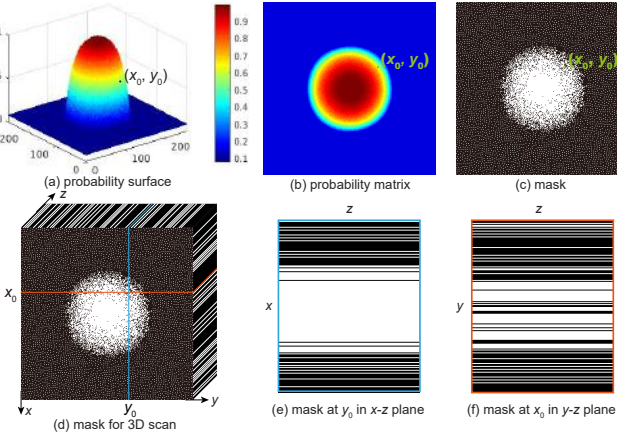


Fig. 16. Our optimal probability matrix and sampling matrix under sampling rate 20%. The 3D view of our undersampling pattern is given, where y, z are two phase encoding directions and x is the frequency encoding direction

Compared with the Gaussian undersampling pattern [38] (Fig. 6e) and the Poisson undersampling pattern [39] (Fig. 6f), our probability matrix and sampling matrix are first initialized randomly, then directly obtained by training real fully-sampled k -space data, instead of defining a specific probability function previously (Gaussian or Poisson), which may not be suitable for different kinds of MR images. Without the quality of MR images as the feedback indicator to progressively adjust the 2D probability function during training, the generalization capability of Gaussian or Poisson function will be fairly poor, and their corresponding patterns are not optimal either.

VI. CONCLUSION AND FUTURE WORK

In this paper, we have proposed a cross-domain network for MR image reconstruction, which contains a 2D probabilistic undersampling layer, a 2D inverse Fourier transform layer, and a reconstruction network. Our method is trained in a retrospective data-driven fashion, under various sampling rates. Thus, we can simultaneously obtain the optimal undersampling pattern (in k -space) and the reconstruction model. The 2D probabilistic undersampling layer, with differentiable probability and sampling matrices, can generate the optimal undersampling pattern and its probability distribution, customized to specific k -space data. The 2D inverse Fourier transform layer connects the Fourier domain and the image domain during the forward pass and backpropagation. By training 3D fully-sampled k -space data and MR images with the traditional Euclidean loss, we have discovered the universal relationship between the probability function of the optimal undersampling pattern (sampling matrix) and its target sampling rate. Experimental results verify that the quality of recovered MR images by our 2D probabilistic undersampling pattern is apparently better than those of existing undersampling methods.

However, there are several underlying directions for further researches:

1) We do not discuss in detail about the balance between the undersampling loss L_{IFT} and the reconstruction loss L_{rec} . We only presume they have the same effect ($\lambda_1 = \lambda_2 = 1$). In

the latter work, we may consider how to effectively combine two losses to further improve the quality of MR images.

2) To obtain universal probability functions, we only use the conventional Euclidean loss to train our cross-domain model. In recent deep learning-based researches, some new types of losses (e.g., perceptual loss) have been proposed. This inspires us to use them to obtain special probability functions.

3) In our experiments, we only use a small amount of 3T and 7T 3D MR k -space data. In the latter work, we will use more k -space data from different positions (e.g., shoulder or knee) and various magnetic fields (e.g., 0.5T or 1.5T), to further prove the robustness of our undersampling pattern and the universality of our probability function.

REFERENCES

- [1] S. Osher, M. Burger, D. Goldfarb, J. Xu, and W. Yin, "An iterative regularization method for total variation-based image restoration," *Multiscale Modeling & Simulation*, vol. 4, no. 2, pp. 460–489, 2005.
- [2] H. Jung, J. Yoo, and J. Ye, "Generalized k-t BLAST and k-t SENSE using FOCUSS," in *IEEE 4th International Symposium on Biomedical Imaging*. IEEE, 2007, pp. 145–148.
- [3] G. Ongie and M. Jacob, "A fast algorithm for structured low-rank matrix recovery with applications to undersampled MRI reconstruction," in *IEEE 13th International Symposium on Biomedical Imaging (ISBI)*. Prague: IEEE, apr 2016, pp. 522–525.
- [4] L. Sun, J. Chen, D. Zeng, and X. Ding, "A novel nonlocal MRI reconstruction algorithm with patch-based low rank regularization," in *IEEE Global Conference on Signal and Information Processing*. IEEE, dec 2015, pp. 398–402.
- [5] E. J. Candes, X. Li, Y. Ma, and J. Wright, "Robust principal component analysis," *Journal of the ACM*, vol. 58, no. 3, p. 11, 2011.
- [6] J. Wright, A. Ganesh, S. Rao, Y. Peng, and Y. Ma, "Robust principal component analysis: exact recovery of corrupted low-rank matrices via convex optimization," in *Advances in Neural Information Processing Systems*, 2009, pp. 2080–2088.
- [7] S. Xue, W. Qiu, F. Liu, and X. Jin, "Low-rank tensor completion by truncated nuclear norm regularization," in *24th International Conference on Pattern Recognition (ICPR)*. Beijing, China: IEEE, aug 2018, pp. 2600–2605.
- [8] S. Xue and X. Jin, "Robust classwise and projective low-rank representation for image classification," *Signal, Image and Video Processing*, vol. 12, no. 1, pp. 107–115, jan 2018.
- [9] M. Aharon, M. Elad, and A. Bruckstein, "K-SVD: an algorithm for designing overcomplete dictionaries for sparse representation," *IEEE Transactions on Signal Processing*, vol. 54, no. 11, pp. 4311–4322, 2006.
- [10] M. Manimala, C. Naidu, and M. N. Giriprasad, "Sparse recovery algorithms based on dictionary learning for MR image reconstruction," in *International Conference on Wireless Communications, Signal Processing and Networking*. IEEE, mar 2016, pp. 1354–1360.
- [11] S. Ravishankar and Y. Bresler, "MR image reconstruction from highly undersampled k -space data by dictionary learning," *IEEE Transactions on Medical Imaging*, vol. 30, no. 5, pp. 1028–1041, 2011.
- [12] H. Bristow, A. Eriksson, and S. Lucey, "Fast convolutional sparse coding," in *IEEE Conference on Computer Vision and Pattern Recognition*, S. Ourselin, L. Joskowicz, M. R. Sabuncu, G. Unal, and W. Wells, Eds. Cham: IEEE, jun 2013, pp. 391–398.
- [13] L. Sun, Z. Fan, Y. Huang, X. Ding, and J. Paisley, "Compressed sensing MRI using a recursive dilated network," in *32nd AAAI Conference on Artificial Intelligence*, 2017, pp. 2444–2451.
- [14] D. Lee, J. Yoo, S. Tak, and J. C. Ye, "Deep residual learning for accelerated MRI using magnitude and phase networks," *IEEE Transactions on Biomedical Engineering*, vol. 65, no. 9, pp. 1985–1995, sep 2018.
- [15] C. M. Hyun, H. P. Kim, S. M. Lee, S. Lee, and J. K. Seo, "Deep learning for undersampled MRI reconstruction," *Physics in Medicine and Biology*, vol. 63, no. 13, p. 135007, 2018.
- [16] G. Yang, S. Yu, H. Dong, G. Slabaugh, P. L. Dragotti, X. Ye, F. Liu, S. Arridge, J. Keegan, Y. Guo, and D. Firmin, "DAGAN: deep de-aliasing generative adversarial networks for fast compressed sensing MRI reconstruction," *IEEE Transactions on Medical Imaging*, vol. 37, no. 6, pp. 1310–1321, jun 2018.

- [17] T. M. Quan, T. Nguyen-Duc, and W. K. Jeong, "Compressed sensing MRI reconstruction using a generative adversarial network with a cyclic loss," *IEEE Transactions on Medical Imaging*, vol. 37, no. 6, pp. 1488–1497, 2018.
- [18] S. Wang, Z. Su, L. Ying, X. Peng, S. Zhu, F. Liang, D. Feng, and D. Lian, "Accelerating magnetic resonance imaging via deep learning," in *International Symposium on Biomedical Imaging*. IEEE, 2016, pp. 514–517.
- [19] J. Schlemper, J. Caballero, J. V. Hajnal, A. Price, and D. Rueckert, "A deep cascade of convolutional neural networks for MR image reconstruction," in *International Conference on Information Processing in Medical Imaging*, M. Niethammer, M. Styner, S. Aylward, H. Zhu, I. Ooguz, P.-T. Yap, and D. Shen, Eds. Cham: Springer International Publishing, 2017, pp. 647–658.
- [20] B. Zhu, J. Z. Liu, S. F. Cauley, B. R. Rosen, and M. S. Rosen, "Image reconstruction by domain-transform manifold learning," *Nature*, vol. 555, no. 7697, pp. 487–492, 2018.
- [21] I. Okusuz, J. Clough, A. Bustin, G. Cruz, C. Prieto, R. Botnar, D. Rueckert, J. A. Schnabel, and A. P. King, "Cardiac MR motion artefact correction from k-space using deep learning-based reconstruction," in *International Workshop on Machine Learning for Medical Image Reconstruction*, F. Knoll et al., Ed. Springer, 2018, pp. 21–29.
- [22] Y. Han, L. Sunwoo, and J. C. Ye, "k-space deep learning for accelerated MRI," *IEEE Transactions on Medical Imaging*, vol. 39, no. 2, pp. 377–386, feb 2020.
- [23] J. Zhang and B. Ghanem, "ISTA-Net: interpretable optimization-inspired deep network for image compressive sensing," in *IEEE Conference on Computer Vision and Pattern Recognition*, 2018, pp. 1828–1837.
- [24] S. Pereira, A. Pinto, V. Alves, and C. A. Silva, "Brain tumor segmentation using convolutional neural networks in MRI images," *IEEE Transactions on Medical Imaging*, vol. 35, no. 5, pp. 1240–1251, 2016.
- [25] H.-C. Shin, H. R. Roth, M. Gao, L. Lu, Z. Xu, I. Nogues, J. Yao, D. Mollura, and R. M. Summers, "Deep convolutional neural networks for computer-aided detection: CNN architectures, dataset characteristics and transfer learning," *IEEE Transactions on Medical Imaging*, vol. 35, no. 5, pp. 1285–1298, 2016.
- [26] K. Bahrami, F. Shi, X. Zong, H. W. Shin, H. An, and D. Shen, "Reconstruction of 7T-like images from 3T MRI," *IEEE Transactions on Medical Imaging*, vol. 35, no. 9, pp. 2085–2097, 2016.
- [27] Y. Yang, J. Sun, H. Li, and Z. Xu, "ADMM-Net: a deep learning approach for compressive sensing MRI," *arXiv Preprint*, vol. 1705.06869, pp. 1–14, 2017.
- [28] O. Ronneberger, P. Fischer, and T. Brox, "U-Net: convolutional networks for biomedical image segmentation," in *International Conference on Medical Image Computing and Computer-Assisted Intervention*, N. Navab, J. Hornegger, W. M. Wells, and A. F. Frangi, Eds. Cham: Springer International Publishing, 2015, pp. 234–241.
- [29] M. Mardani, E. Gong, J. Y. Cheng, S. S. Vasanawala, G. Zaharchuk, L. Xing, and J. M. Pauly, "Deep generative adversarial neural networks for compressive sensing (GANCS) MRI," *IEEE Transactions on Medical Imaging*, vol. 38, no. 1, pp. 167–179, jan 2019.
- [30] J.-Y. Zhu, T. Park, P. Isola, and A. A. Efros, "Unpaired image-to-image translation using cycle-consistent adversarial networks," in *IEEE International Conference on Computer Vision*. IEEE, oct 2017, pp. 2242–2251.
- [31] B. Gözcü, R. K. Mahabadi, Y.-H. Li, E. Ilicak, T. Cukur, J. Scarlett, and V. Cevher, "Learning-based compressive MRI," *IEEE Transactions on Medical Imaging*, vol. 37, no. 6, pp. 1394–1406, jun 2018.
- [32] I. A. Huijben, B. S. Veeling, and R. J. van Sloun, "Deep probabilistic subsampling for task-adaptive compressed sensing," in *International Conference for Learning Representations*, 2020, pp. 1–16.
- [33] H. K. Aggarwal and M. Jacob, "J-MoDL: joint model-based deep learning for optimized sampling and reconstruction," *arXiv Preprint*, vol. 1911.02945, pp. 1–10, 2019.
- [34] T. Weiss, S. Vedula, O. Senouf, O. Michailovich, M. Zibulevsky, and A. Bronstein, "Joint learning of Cartesian undersampling and reconstruction for accelerated MRI," in *IEEE International Conference on Acoustics, Speech and Signal Processing (ICASSP)*. IEEE, may 2020, pp. 8653–8657.
- [35] C. D. Bahadir, A. V. Dalca, and M. R. Sabuncu, "Learning-based optimization of the undersampling pattern in MRI," in *International Conference on Information Processing in Medical Imaging*, vol. 12, no. 6. Springer, 2019, pp. 780–792.
- [36] D. P. Kingma and J. Ba, "Adam: a method for stochastic optimization," in *International Conference for Learning Representations*, San Diego, dec 2015, pp. 1–13.
- [37] M. Abadi, P. Barham, J. Chen, Z. Chen, A. Davis, and J. Dean, "Tensorflow: A system for large-scale machine learning," in *12th USENIX Symposium on Operating Systems Design and Implementation (OSDI)*, 2016, pp. 265–283.
- [38] R. L. Cook, "Stochastic sampling in computer graphics," *ACM Transactions on Graphics (TOG)*, vol. 5, no. 1, pp. 51–72, jan 1986.
- [39] T. R. Jones, "Efficient generation of Poisson-disk sampling patterns," *Journal of Graphics Tools*, vol. 11, no. 2, pp. 27–36, jan 2006.
- [40] L. Liu, G. Zheng, J. D. Bastian, M. J. B. Keel, L. P. Nolte, K. A. Siebenrock, and T. M. Ecker, "Periacetabular osteotomy through the pararectus approach: technical feasibility and control of fragment mobility by a validated surgical navigation system in a cadaver experiment," *International Orthopaedics*, vol. 40, no. 7, pp. 1389–1396, jul 2016.
- [41] S. Bakas, H. Akbari, A. Sotiras, M. Bilello, M. Rozycski, J. S. Kirby, J. B. Freymann, K. Farahani, and C. Davatzikos, "Advancing the cancer genome atlas glioma MRI collections with expert segmentation labels and radiomic features," *Scientific Data*, vol. 4, p. 170117, sep 2017.
- [42] Z. Wang, A. Bovik, H. Sheikh, and E. Simoncelli, "Image quality assessment: from error visibility to structural similarity," *IEEE Transactions on Image Processing*, vol. 13, no. 4, pp. 600–612, apr 2004.